








# New dynamic diamond anvil cells for tera-pascal per second fast compression x-ray diffraction experiments

Cite as: Rev. Sci. Instrum. **90**, 065114 (2019); <https://doi.org/10.1063/1.5098993>

Submitted: 05 April 2019 . Accepted: 27 May 2019 . Published Online: 21 June 2019

Zs. Jenei , H. P. Liermann , R. Husband, A. S. J. Méndez, D. Pennicard, H. Marquardt, E. F. O'Bannon , A. Pakhomova, Z. Konopkova, K. Glazyrin , M. Wendt, S. Wenz, E. E. McBride , W. Morgenroth , B. Winkler, A. Rothkirch, M. Hanfland, and W. J. Evans 



View Online



Export Citation



CrossMark

## ARTICLES YOU MAY BE INTERESTED IN

[A modular, multi-diagnostic, automated shock tube for gas-phase chemistry](#)

Review of Scientific Instruments **90**, 064104 (2019); <https://doi.org/10.1063/1.5095077>

[Contributed Review: Culet diameter and the achievable pressure of a diamond anvil cell: Implications for the upper pressure limit of a diamond anvil cell](#)

Review of Scientific Instruments **89**, 111501 (2018); <https://doi.org/10.1063/1.5049720>

[Dynamic diamond anvil cell \(dDAC\): A novel device for studying the dynamic-pressure properties of materials](#)

Review of Scientific Instruments **78**, 073904 (2007); <https://doi.org/10.1063/1.2751409>



### AVS Quantum Science

A high impact interdisciplinary journal for **ALL** quantum science



ACCEPTING SUBMISSIONS

# New dynamic diamond anvil cells for tera-pascal per second fast compression x-ray diffraction experiments

Cite as: Rev. Sci. Instrum. 90, 065114 (2019); doi: 10.1063/1.5098993

Submitted: 5 April 2019 • Accepted: 27 May 2019 •

Published Online: 21 June 2019



View Online



Export Citation



CrossMark

Zs. Jenei,<sup>1,a)</sup>  H. P. Liermann,<sup>2</sup>  R. Husband,<sup>2</sup> A. S. J. Méndez,<sup>2</sup> D. Pennicard,<sup>2</sup> H. Marquardt,<sup>3</sup> E. F. O'Bannon,<sup>1</sup>  A. Pakhomova,<sup>2</sup> Z. Konopkova,<sup>2,4</sup> K. Glazyrin,<sup>1</sup>  M. Wendt,<sup>2</sup> S. Wenz,<sup>2</sup> E. E. McBride,<sup>2,b)</sup>  W. Morgenroth,<sup>5</sup>  B. Winkler,<sup>5</sup> A. Rothkirch,<sup>2</sup> M. Hanfland,<sup>6</sup> and W. J. Evans<sup>1</sup> 

## AFFILIATIONS

<sup>1</sup>High Pressure Physics Group, Lawrence Livermore National Laboratory, 7000 East Avenue, L-041, Livermore, California 94550, USA

<sup>2</sup>Photon Science, DESY, Notkestrasse 85, 22607 Hamburg, Germany

<sup>3</sup>Department of Earth Sciences, University of Oxford, South Parks Road, OX1 3AN Oxford, United Kingdom

<sup>4</sup>European X-Ray Free-Electron Laser Facility GmbH, Holzkoppel 4, 22869 Schenefeld, Germany

<sup>5</sup>Arbeitsgruppe Kristallographie, Department of Geoscience, University of Frankfurt, 60438 Frankfurt, Germany

<sup>6</sup>ESRF, The European Synchrotron, 71 Avenue des Martyrs, 38000 Grenoble, France

<sup>a)</sup> Author to whom correspondence should be addressed: [jeneizs@llnl.gov](mailto:jeneizs@llnl.gov)

<sup>b)</sup> Current address: SLAC National Accelerator Laboratory, 2575 Sand Hill Rd., Menlo Park, California 94025, USA.

## ABSTRACT

Fast compression experiments performed using dynamic diamond anvil cells (dDACs) employing piezoactuators offer the opportunity to study compression-rate dependent phenomena. In this paper, we describe an experimental setup which allows us to perform time-resolved x-ray diffraction during the fast compression of materials using improved dDACs. The combination of the high flux available using a 25.6 keV x-ray beam focused with a linear array of compound refractive lenses and the two fast GaAs LAMBDA detectors available at the Extreme Conditions Beamline (P02.2) at PETRA III enables the collection of x-ray diffraction patterns at an effective repetition rate of up to 4 kHz. Compression rates of up to 160 TPa/s have been achieved during the compression of gold in a 2.5 ms fast compression using improved dDAC configurations with more powerful piezoactuators. The application of this setup to low-Z compounds at lower compression rates is described, and the high temporal resolution of the setup is demonstrated. The possibility of applying finely tuned pressure profiles opens opportunities for future research, such as using oscillations of the piezoactuator to mimic propagation of seismic waves in the Earth.

Published under license by AIP Publishing. <https://doi.org/10.1063/1.5098993>

## I. INTRODUCTION

For many decades, the diamond anvil cell (DAC) has been the primary technique used for the application of static high pressures, enabling researchers to explore the physics and chemistry of compounds at multimegabar pressure.<sup>1</sup> The transparency of the diamond anvils over a wide range of wavelengths provides access to the sample for numerous experimental techniques such as spectroscopic techniques (Raman, fluorescence, infrared, and x-ray) and both single crystal and powder x-ray diffraction techniques.

Quasihydrostatic conditions can be achieved through the use of pressure-transmitting media such as inert gases<sup>2,3</sup> or by annealing of the sample after compression.<sup>4</sup>

However, the use of the DAC to dynamically compress materials was mostly neglected until the invention of the dynamic diamond anvil cell (dDAC).<sup>5</sup> In this device, the expansion of a voltage-driven piezoactuator is used to apply force to the back side of the DAC. Since its conception, this device led to the realization that dynamically driven DACs, by means of a membrane or a piezoactuator, can be used to investigate compression-rate dependent phenomena

(e.g., 1st and 2nd order phase transitions) as well as metastable states of matter<sup>6,7</sup> created by overdriving the pressure across the equilibrium phase boundary. More recently, it was realized that this technique can also be used to study compression processes on the atomistic scale that occur during meteorite impacts on the surface of the Earth or other planetary bodies.<sup>8–11</sup>

Time-resolved x-ray diffraction experiments have been reported; most of these experiments follow the crystal structure evolution of materials along a defined compression pathway in dynamically driven DACs.<sup>12–15</sup> These experiments have mostly been confined to lower compression rates since neither the intensity of the incident beam at 3rd generation light sources nor the repetition rate and sensitivity of the available detectors have been sufficient to offer the time resolution required at higher compression rates.<sup>16,17</sup> Thus, many fast-compression experiments have relied on alternative diagnostics such as fast microphotography<sup>6</sup> or fast Raman spectroscopy<sup>7,18,19</sup> to collect data on the phase changes that occur during fast compression of the sample. While these techniques can identify phase boundaries, they do not provide a direct method to study the crystal structure evolution.

In this paper, we present the fast x-ray diffraction setup and dynamic DACs developed at the Extreme Conditions Beamline (ECB, P02.2) at PETRA III in collaboration with the High Pressure Physics Group at Lawrence Livermore National Laboratory (LLNL) and the Crystallography/Mineralogy group at the University of Frankfurt. The new dDAC platforms are able to reach compression rates on the order of  $10^2$  TPa/s with either a symmetric piston cylinder or LLNL-type DAC, while simultaneously following the crystal structure evolution of the compressed sample using fast (4 kHz) time-resolved powder x-ray diffraction. This has been achieved by combining the improved dDAC technology with the brilliant x-ray source at PETRA III, tuned to 25.6 keV, and the newly developed GaAs LAMBDA detectors.<sup>20</sup>

## II. EXPERIMENTAL METHOD

### A. Dynamic diamond anvil cell developments at LLNL

The latest dDAC developments at LLNL have their roots in the original design by Evans *et al.*<sup>5</sup> In this section, the two distinct dDAC designs that have been developed at LLNL are presented, both of which were designed around the LLNL-designed membrane DAC described in Ref. 21. The first design is based on the original 3-piezo-dDAC design by Evans *et al.*, which has been modified to achieve higher forces than the original setup. Second, a new 1-piezoconfiguration has been developed.

The scope of the development was to create a dynamic compression device that can achieve higher pressures and thus compression rates than the previous designs. Diamond anvils used in DACs can withstand opposing forces of around 15–16 kN. At these forces, the pressure in the sample chamber can reach up to 3 Mbar, depending on the culet diameter.<sup>22</sup> When selecting piezoactuators for the new dDACs, we worked under the assumption that the gasket thickness at the start of the experiment was 20–25  $\mu\text{m}$ , reaching a minimum thickness of 5  $\mu\text{m}$  at the maximum pressure at which point the stiffness of the gasket was assumed to be infinite. This would enable an  $\sim 15$ –20  $\mu\text{m}$  expansion of the piezo during the compression experiment. Thus, the force at the end of the expansion

should be equal to the force that is typically applied to the anvil just before the diamonds fail. This ensures that the design can reach pressures commonly achieved in a conventional DAC which would use a membrane or screws to apply force to the anvils.

Limitations on the design are imposed by the dimensions of the experimental setup, i.e., the dDAC assembly must fit between the focus point of the x-ray beam and the focusing optics. Also, one has to take into account the use of pinholes to decrease the intensity in the tails of the focused x-ray beam. Piezoactuators with a length of less than 75 mm were therefore selected. Taking into account the  $\sim 15$ –20  $\mu\text{m}$  expansion of the piezo, the choices for off-the-shelf piezoactuators were limited. The 72 mm hollow cylinder design with the Piezosystem Jena HPSt 1000/35-25/80 piezoactuator was chosen for the 1-piezoconfiguration and the 71 mm pretensioned Piezosystem Jena PSt 1000/16/60 VS25 actuators for the 3 piezoconfiguration.

For dynamic compression experiments, another important consideration is the time required to reach the desired pressure. The piezoactuator can be modeled as a capacitor, where a certain amount of electric charge has to be delivered from the power supply in order for the piezo to expand. Thus, the higher the power of the power supply (in this case an amplifier), the faster the piezoactuator will expand. The commercially available Piezosystem Jena HV RCV1000/7 amplifier delivers a peak current of 7 A and proves to be the most suitable for the above piezoactuators. With this amplifier, the nominal electronic rise time for the hollow cylinder (HPSt 1000/35-25/80) actuator is  $\sim 370$   $\mu\text{s}$  for an expansion of 20  $\mu\text{m}$  and  $\sim 450$   $\mu\text{s}$  for the 3-piezo configuration. Thus, the maximum pressure can nominally be reached within less than half a millisecond, where the maximum force at the end of expansion should be enough to compress the samples to the maximum pressures attainable with the given diamond anvil pair. The use of this amplifier enables seamless integration into the existing experimental setup at the ECB.

Schematic diagrams illustrating the two different piezoassemblies are shown in Fig. 1. The new 1-piezo-dDAC design (Fig. 1, left panel) consists of a Vascomax hardened steel cylinder, where the DAC is screwed into one end of the cylinder and the HPSt 1000/35-25/80 piezoactuator inserted into the opposite end. The piezoactuator is then pressed against the DAC by tightening the cap on the opposing side until the piezoactuator engages (i.e., the pressure in the sample chamber slightly increases). The right panel in Fig. 1 shows the cross section of the three-piezoconfiguration that is very similar to the original dDAC setup by Evans *et al.*,<sup>5</sup> but with enhanced capabilities. The PSt 1000/16/60 VS25 pretensioned actuators are capable of delivering 15–18 kN force and a 15–20  $\mu\text{m}$  expansion. Additionally, this configuration contains a membrane that can be used independently from the piezoactuators. The specifications and calculated rise times of the piezoactuators are given in Table I.

### B. Dynamic diamond anvil cell developments from beamline P02.2 at PETRA III

The aim of the dDAC development at PETRA III was to provide a driver that can be interfaced with different types of DACs commonly employed by the high-pressure community.<sup>17,23</sup> The setup uses symmetric piston cylinder type DACs,<sup>1</sup> which are equipped on the downstream side with cubic boron nitride

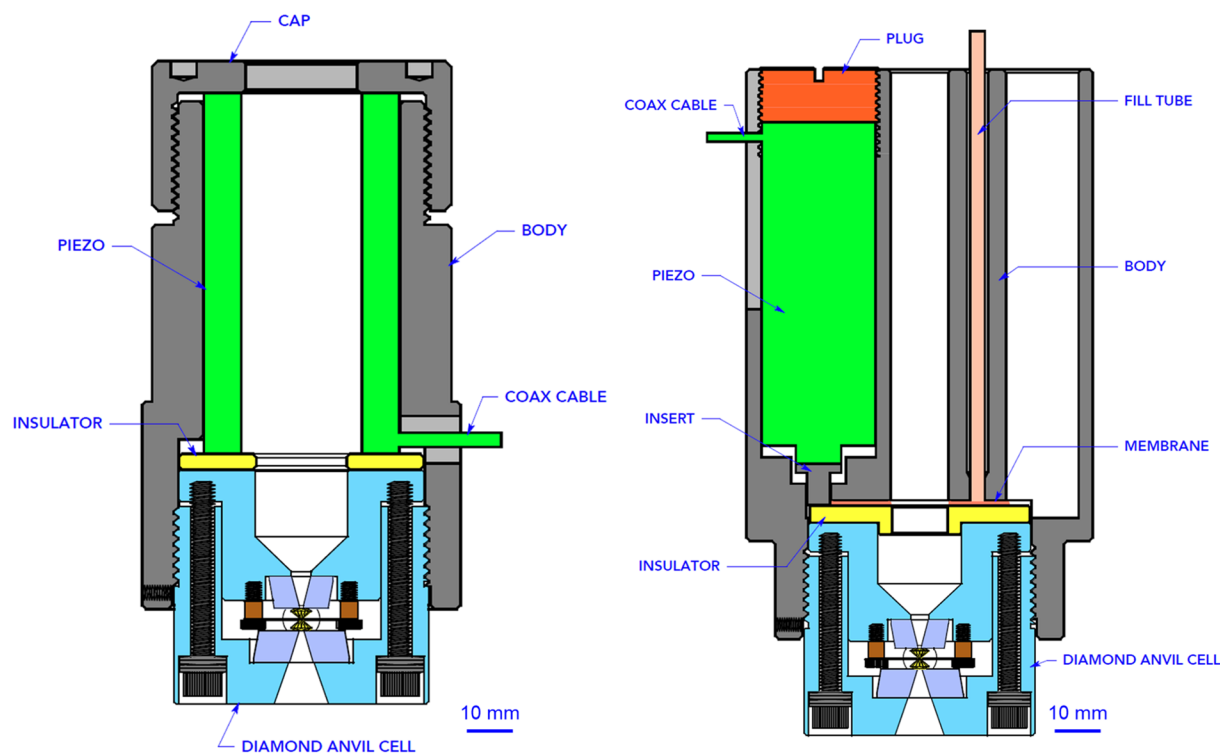


**FIG. 1.** LLNL dDAC assemblies. Left: 1-piezoconfiguration with the hollow cylinder piezoactuator. Right: 3 piezoconfiguration, incorporating a membrane that can be used to set an arbitrary starting pressure for the compression. The piezoactuator is shown in green, the assembly body in gray, and the LLNL piston cylinder cell in blue.

(c-BN) and on the upstream side with tungsten carbide seats, both of which offer a visible light optical opening angle of  $\pm 28^\circ$  and an x-ray opening of  $\pm 35^\circ$ . An overview of the ECB dDAC design is shown in Fig. 2. The DAC is enclosed by a cylinder of hardened steel (Type 1.4112) that is open at one end. The piezoactuator sits at the upstream end of the cylinder so that it pushes directly on the DAC. The upstream end of the cylinder is closed through an end cap with fine threading, which applies a small pressure to the piezoactuator and precompresses the sample.

The choice of piezoactuator was influenced by the same considerations discussed in the description of the LLNL dDAC described above. This resulted in the choice of piezostack actuators with different lengths of 60 mm (type 72-285 from PI Ceramic GmbH) and 90 mm (64-107 from PI Ceramic GmbH), details of which are given in Table I. These piezoactuators have a through-hole of 9 mm in diameter, which allows the sample to be rotated  $\pm 1^\circ$  on the sample stack in the x-ray beam. Each piezoactuator has its own dDAC housing of the appropriate dimensions, and the choice of the actuator is dependent on the needs of the particular experiment. For example, while the larger piezo can provide more force, the smaller piezo offers a shorter rise time and has the advantage that the pinhole can be placed closer to the sample, enabling a cleaner focus (less tail) of the x-ray beam on the sample.

The piezoactuators chosen for the ECB dDAC have a much larger contact area with the DAC than the hollow cylinder piezo used in the LLNL design. Consequently, in the ECB configuration, the

force applied to the DAC is critically dependent on the parallelism at the interfaces between the dDAC housing, the DAC, and the piezoactuator, as any gaps will have to be compensated through the extension of the piezoactuator (thus reducing the maximum force that can be applied to the diamond anvils). Furthermore, an uneven force distribution across the piezo can cause mechanical damage to the piezoceramic disks, causing the material to fracture and potential electrical breakdown. In the final design, unevenness has almost completely been eliminated and force is lost only in piezo-expansion due to the thinning of the metal gasket as described in Sec. II A.

Due to the uncertainty in the parallel alignment, in the thinning of the gasket, and in the precompression applied by tightening the cap, it is not possible to precisely determine the force applied to the DAC. Pressure vs applied voltage curves for the 90 mm and 60 mm piezoactuators performed using deionized water as a test sample are shown in Figs. 3 and 12–14. The tests were performed using diamond anvils with a range of culet sizes (50–300  $\mu\text{m}$ ), and the DACs were equipped with Re gaskets which were preindented to an initial thickness of 20–25  $\mu\text{m}$ . For some tests, a small ruby sphere ( $< 5 \mu\text{m}$ ) was included for pressure calibration. Pressure was determined either by applying the ruby fluorescence method according to the calibration by Dewaele *et al.*,<sup>24</sup> or by using the Raman shift of the diamond anvil in the stressed region according to the calibration by Akahama and Kawamura.<sup>25</sup> The maximum pressure achieved for a given culet size is equal to the pressure limit in a

**TABLE I.** Specifications of the amplifiers and piezoactuators employed to drive the symmetric DAC and LLNL membrane dDACs. Electronic rise times for the piezoactuators are the theoretical values calculated with the added 50% capacitance for the large signal variation (0–1 kV).

Piezoactuator	72-285 <sup>a</sup> ECB	64-107 <sup>a</sup> ECB	HPSt 1000/35-25/80 <sup>b</sup> LLNL	3× PSt 1000/16/60 VS25 <sup>b</sup> LLNL
Capacity ( $\mu\text{F}$ )	7.46	11/16.5	1.3	1.62
Blocking force (N)	71	71	20	36
Diameter/length (mm)	56/60	56/90	35/72	3× 16/71

Amplifier	Peak current (A)	Repetition rate (Hz)	Required capacity	Minimum rising time ( $10^{-3}$ s)			
HV-RCV1000/3 <sup>b</sup>	3	200	Requested	3.73	5.50	0.650	0.810
HV-RCV1000/7 <sup>b</sup>	7	200	>2000 nF	1.60	2.36, 2.50 <sup>c</sup>	0.279, 0.340 <sup>d</sup>	0.347, 0.450 <sup>d</sup>
HVP 1000/20 <sup>b</sup>	20	10	>2000 nF	0.56	0.83	0.098	0.121

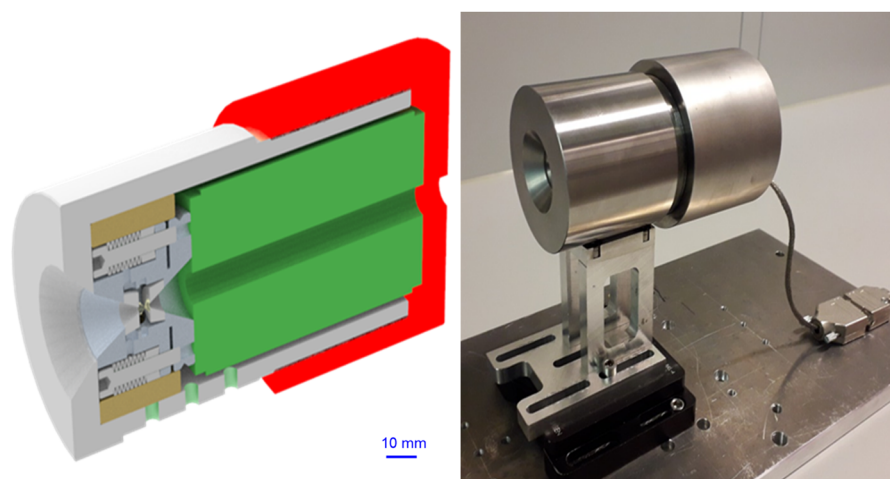
<sup>a</sup>PI Ceramic GmbH.<sup>b</sup>Piezosystems Jena GmbH.<sup>c</sup>Measured rise time.<sup>d</sup>Manufacturer calculated rise time.

conventional DAC. In particular, we would like to highlight the test using  $50\ \mu\text{m}$  culets, in which the sample was compressed from a starting pressure of  $\sim 9$  GPa to  $\sim 203$  GPa at the maximum voltage. Similar test experiments were carried out with stainless steel gaskets with both the small and large piezoassemblies. For compression ramps below 1 Mbar, stainless steel has the advantage that the sample pressure generally reverts to the initial value after the experiment, allowing for each sample to be compressed multiple times (see Fig. 14 in the Appendix). However, for compressions above 1 Mbar, Re has been found to be a more stable gasket material (i.e., the gasket hole remains centered and does not blow out). The results from these additional tests are shown in the Appendix (Figs. 12–14). It should be noted that the pressure vs applied voltage curve is dependent on the compressibility of the sample, pressure medium, and gasket material and so will not be the same when compressing different samples.

Pressure vs applied voltage curves for deionized water were also measured for the 1-piezo-LLNL dDAC using diamonds with  $300\ \mu\text{m}$  culets. The results are very similar to the compression curve for the small ECB piezoactuator for diamonds of the same culet size. At 990 V, the sample pressure was 48 GPa and 40 GPa for the small ECB piezoactuator and 1-piezo-LLNL assemblies, respectively.

### C. dDAC drive and control for fast X-ray diffraction experiments

Both the LLNL and ECB dDACs are driven by the same control system based on the block diagram shown in Fig. 4. It consists of a waveform generator (Agilent 33522B), a delay generator (SRS, DG645/5 with Rb clock), and the piezoamplifier (Piezosystem Jena GmbH). The arbitrary waveform, which is typically trapezoidal with user-defined rise, hold, and fall times can be tailored to suit

**FIG. 2.** Left: 3D model of the dDAC developed at the ECB, DESY. Right: Photo of the dDAC equipped with the large piezoactuator (90 mm in length).



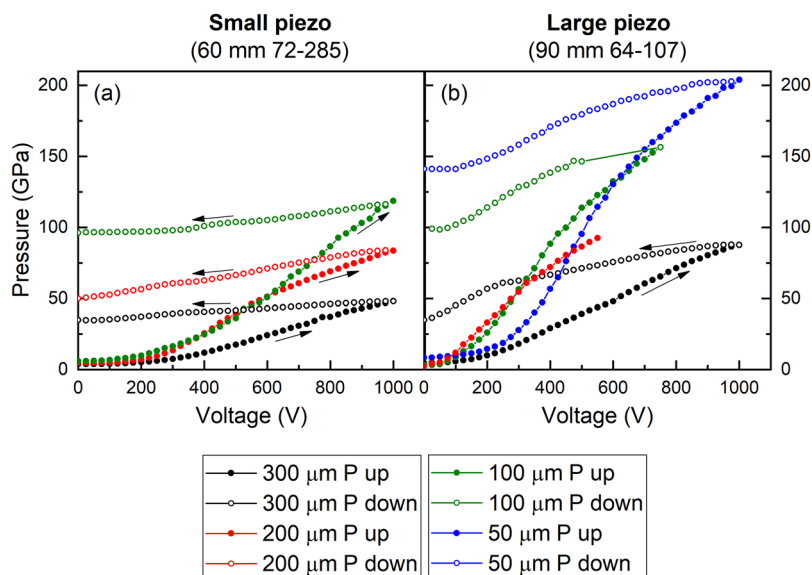


**FIG. 3.** Plot of pressure vs applied voltage for a water sample on compression and decompression in the ECB dDAC using the small (a) and large (b) piezoactuators for diamond anvils with different culet sizes. In most cases, the pressure was determined using the fluorescence of a small ruby sphere ( $\sim 5 \mu\text{m}$ ) included in the sample chamber employing the calibration by Dewaele *et al.*<sup>24</sup> For the  $50 \mu\text{m}$  culet diamonds, the pressure was determined from the Raman shift of the diamond phonon from the stressed region using the calibration by Akahama and Kawamura.<sup>25</sup>

the experimental needs via the Agilent Benchlink waveform builder software by Keysight. The waveform is sent via universal serial bus (USB) connection to the waveform generator. The delay generator is triggered by an I/O signal controlled by the beamline control computer and this signal also triggers the recording of the drive signals on digital oscilloscopes. The timing of the experiment is determined by the delay generator, which allows for a time delay between the I/O signal and the triggering of each of the two LAMBDA detectors and the waveform generator which can all be set independently. For the highest time resolution, both LAMBDA detectors are operated at the same acquisition frequency (2 kHz), but with their triggering offset by 0.25 ms (half the exposure time of a single LAMBDA detector) resulting in an effective frequency of 4 kHz at 12bit data collection mode.

### III. GaAs LAMBDA DETECTOR

The GaAs LAMBDA detector is a photon counting x-ray detector using gallium arsenide as a sensor material.<sup>20</sup> The system is

composed of 3 modules which are tiled together resulting in an image of a total of approx. 2.3 megapixels with a pixel size of  $55 \mu\text{m}$  and a sensitive area of  $8.5 \text{ cm} \times 8.5 \text{ cm}$ . Note that intermodular gaps exists in the full image. The detector has a hybrid pixel structure, with each module having two  $500 \mu\text{m}$ -thick GaAs pixel sensors bonded to a total of 12 Medipix3 readout chips.<sup>26</sup> This combination makes it possible to count individual hard x-ray photons with high detection efficiency (with almost 100% of photons being absorbed at 25.6 keV beam energy). The point spread function of these sensors is close to that of an ideal  $55 \mu\text{m}$  pixel, varying somewhat with the photon energy and threshold setting.<sup>27</sup> Each module has readout electronics with high-speed optical links, allowing the full detector to be read out at 2000 frames/s with no dead time between images (12-bit data collection mode). Because the mechanical alignment of the three modules is less precise than the pixel size, the relative positions of the modules was measured to allow accurate reconstruction of full images. This was achieved by taking x-ray images of a pin-hole mask placed on the detector, and analyzing the positions of the pinholes seen on the different modules.

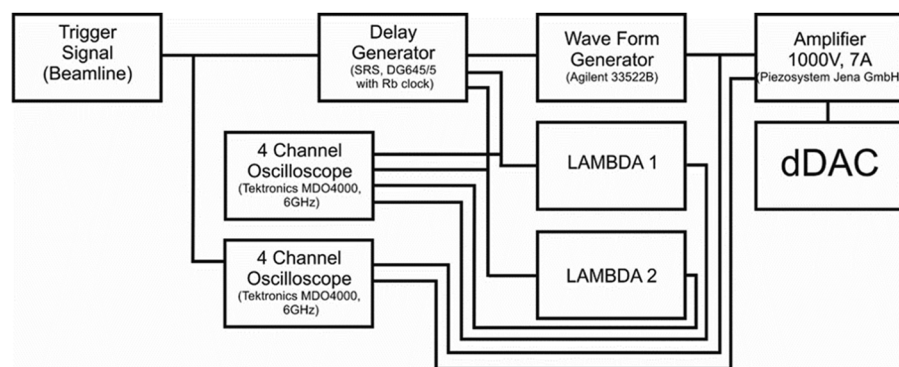


**FIG. 4.** Drive control schematics that are employed at the ECB (P02.2) to operate the different dDAC devices in combination with detecting devices.

At the ECB (P02.2), two 2M GaAs LAMBDA detectors are used simultaneously and positioned independently according to the needs of the experiment. Typically, the detectors are offset in the horizontal direction from the direct beam so that the x-ray beam passes between the two detectors, where the minimum distance between the sensitive areas of each module is  $\sim 130$  mm due to constraints imposed by the size of the detector body. Using a Compound Refractive Focused (CRL) focused beam [ $8(h) \times 2(v) \mu\text{m}^2$  FWHM] each detector can capture up to  $\sim 20\%$  of a Debye Scherrer ring, depending on where it falls on the detector. A calibration procedure was developed to minimize potential issues originating from the partial coverage of the detector. We determined that a  $\text{CeO}_2$  [National Institute of Standards (NIST) 647b] diffraction standard was insufficient since only 5–6 diffraction rings are illuminating each LAMBDA detector at a Sample to Detector Distance (SDD) of 400–450 mm at 25.6 keV. Instead, three diffraction standards with relatively large lattice parameters and minimal peak overlap were chosen ( $\text{Cr}_2\text{O}_3$  from NIST 647b,  $\text{Al}_2\text{O}_3$  from NIST 676a and  $\text{LaB}_6$  from NIST 660c). Powder diffraction patterns of each of the standards were collected separately and each time the standard was rotated  $\pm 5^\circ$  to improve the statistics of the diffraction rings. DIOPTAS software<sup>28</sup> was used to calibrate the SSD, detector tilt, and rotation using primarily the  $\text{Cr}_2\text{O}_3$  (NIST 647b) diffraction pattern with 10 observable diffraction lines at a SDD of 400–450 mm and the energy of 25.6 keV. The calibration was cross checked with the diffraction patterns of  $\text{Al}_2\text{O}_3$  and  $\text{LaB}_6$  provided by the DIOPTAS software. For fast diffraction experiments, the detector was set into the 12-bit mode to increase sensitivity while decreasing the dynamic range of the LAMBDA detectors. For each detector, a flat field correction was applied in the 12-bit mode derived from long homogeneous exposures of a metallic glass at 25.6 keV, the energy used for dynamic driven DAC experiments. Finally, a pixel mask for each detector was created in DIOPTAS to eliminate any hot pixels before integrating the 3D diffraction images. This is absolutely necessary when conducting very fast diffraction/compression experiments where the count rate on the detector is very low.

The quality of the diffraction images of any given detector is not only determined by its physical properties, such as pixel size and point spread function, but ultimately by the Instrumental Resolution Function (IRF) that combines detector characteristics, beamline properties, and sample geometries. The IRF of the GaAs LAMBDA detector was determined using the  $\text{CeO}_2$  standard (NIST 647b) placed in an empty stainless steel gasket hole. Data were collected at 25.6 keV with a CRL focused x-ray beam [ $8(h) \times 2(v) \mu\text{m}^2$  FWHM] at varying SDD. Similar measurements have been performed at the ECB employing a CRL (or KB-Mirror) focused beam with a CsI flat panel detector XRD 1621 from Perkin Elmer.<sup>29</sup> Figure 5 shows the FWHM obtained for different  $\text{CeO}_2$  diffraction peaks measured with the GaAs LAMBDA detector at different SDDs. For comparison, results obtained from measurements carried out with PerkinElmer XRD1621 are given in addition. The plot indicates clearly that the IRF of the GaAs LAMBDA detector is better by a factor of 3 compared to that of the XRD1621. Furthermore, increasing values of the FWHM of the diffraction peak as a function of increasing  $2\theta$  indicates that the IRF is no longer controlled by the pixel size, as shown for the XRD1621, but rather by the divergence of the incident beam.<sup>29</sup>

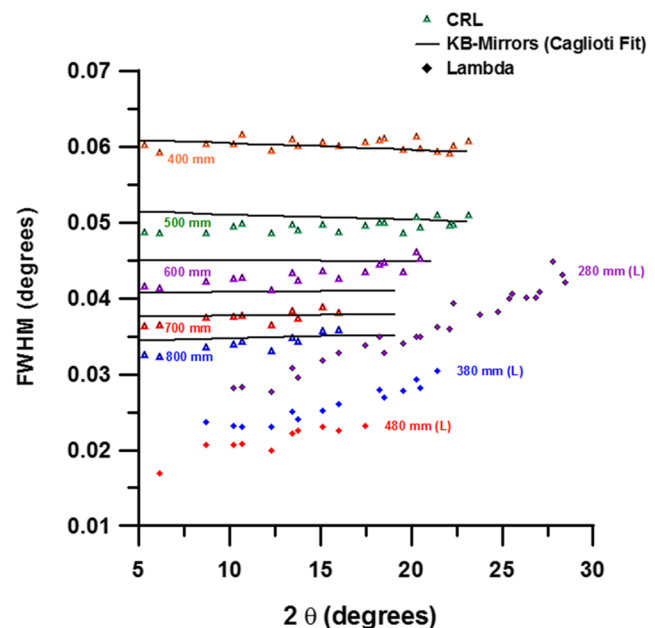


**FIG. 5.** FWHM of the  $\text{CeO}_2$  (NIST) standard collected at the ECB with a Compound Refractive Focused (CRL) beam of 25.6 keV as a function of  $2\theta$  for different Sample to Detector Distances (SDD). Triangles indicate the FWHM of the diffraction peaks of  $\text{CeO}_2$  collected on the CsI XRD 1621 flat panel from Perkin Elmer, while diamonds indicate the FWHM collected on the GaAs LAMBDA detector from X-Spectrum. One can clearly see that the IRF of the GaAs LAMBDA detector is improved by a factor of 3.

This additional feature of the detector will play a significant role in its performance with respect to resolving power as described in later examples.

## IV. RESULTS AND DISCUSSION

### A. Fast compression of high-Z materials I: Gold

In order to determine the maximum compression rate that can be achieved using the improved ECB dDAC design, fast x-ray diffraction experiments were performed on dynamically compressed high-Z elements. In one experiment, a symmetric DAC with 0.05 mm culets was loaded with Au powder (Sigma Aldrich, 326 585), which was loaded into a 0.02 mm hole in a 0.025 mm thick indented gasket. A trapezoidal voltage waveform with 2.5 ms rise, hold and fall times was applied using the small 60 mm piezoactuator, employing the maximum 1000 V from the 7 A amplifier and compressing the Au sample to the maximum pressure in 2.5 ms (Fig. 6). X-ray diffraction patterns were collected using an  $8(h) \times 2(v) \mu\text{m}^2$  x-ray beam tuned to  $\sim 25.6$  keV. During the compression, both LAMBDA detectors collected diffraction images at the maximum frame rate of 2 kHz with a triggering delay of 0.25 ms between the two detectors (to achieve the 4 kHz effective collection rate). At a SDD of 425.7 mm, diffraction peaks on both detectors covered a Q range of 2 to  $4.6 \text{ \AA}^{-1}$ , enough to record the (111) and (200) reflection of Au to the maximum pressure of  $\sim 140$  GPa.

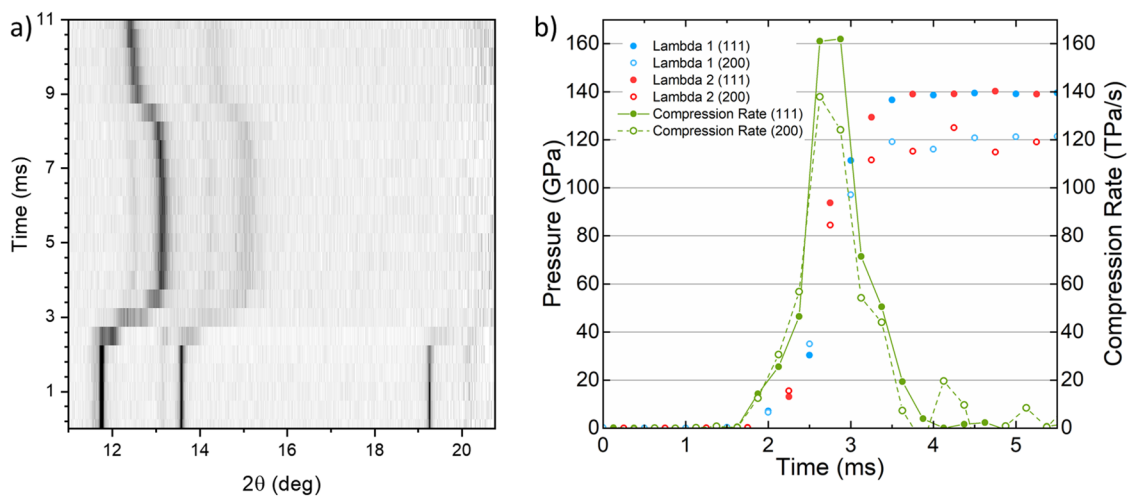


**FIG. 6.** Fast compression experiment of gold to a maximum pressure of  $\sim 140$  GPa in 2.5 ms. (a) Contour plot of the integrated diffraction images collected from one of the GaAs LAMBDA 2M detectors at a frame rate of 2 kHz. (b) Plot of pressure calculated using the EOS of Au by Anderson *et al.*<sup>30</sup> based on the cell parameters and unit cell volume derived from the Au(111) diffraction line. By delaying the triggering of the second detector by 0.25 ms, it was possible to cover the 2.5 ms ramp with 8 data points that indicate that the peak compression rate was around 160 TPa/s.

A contour plot showing the time evolution of the integrated diffraction patterns during the compression experiment and the pressure-time path explored during the compression ramp is shown in Fig. 6. The pressure was calculated using the EOS for Au from Anderson *et al.*<sup>30</sup> and the cell parameter/volume derived from the Au(111) diffraction peak fitted with a pseudo-Voigt function in the program PeakFit©. As the compression occurred under nonhydrostatic conditions, the pressure estimated from the (111) and (200) diffraction peaks deviate significantly at high pressures by as much as 14.3 GPa at 111 GPa (see Fig. 6), this is not unexpected, due to the difference in the line shift.<sup>31</sup> A full analysis of the relative line shift caused by nonhydrostaticity and estimation of the average pressure<sup>32</sup> was not possible due to the lack of diffraction peaks, but will be the subject of future experiments. The compression corresponds to an average compression rate of 56 TPa/s and a maximum compression rate of  $\sim 160$  TPa/s as calculated from the differentiation of the pressure-time curve. Although higher compression rates may be achieved using the larger piezoactuator, it will also result in a lower coverage of the compression ramp with diffraction images and result in inaccurate compression-rate estimations.

We consider this compression rate as the maximum rate at which fast compression experiments of high-Z materials in the dDAC can be performed and data collected at 3rd generation light sources at this time. Faster experiments are limited both by the maximum brilliance available at these light sources and the maximum speed of the detectors. Only at ultralow emittance sources such as the ESRF-EBS, APS-U, and PETRA IV,<sup>33</sup> with smaller emittance and more effective focusing resulting in higher brilliance on the sample, one might be able to collect diffraction images at higher compression rates. Alternatively, one can conduct diffraction experiments at hard x-ray XFELs such as the European XFEL, where detectors such as the AGIPD (Adaptive Gain Integrating Pixel Detector) will be able to operate at frame rate up to 4.5 MHz, which is the pulse repetition frequency in a bunch train of the European XFEL.

## B. Fast compression of high-Z materials II: Bismuth

The strain-rate dependence of phase transitions and/or structural changes at high pressures and temperatures is an active area of research, where the results of dynamic compression experiments such as shock compression are often used to model the conditions in the interior of planetary systems, in which processes occur at comparatively much longer time scales.<sup>34</sup> The dDAC systems described in this paper provide a platform to study the effects of kinetics on solid-solid phase transitions at intermediate strain rates that are not accessible through other techniques. This technique therefore has the potential to greatly contribute to the overall understanding of the influence of compression rate on phase transformations in materials.

Bi is an excellent prototype system to demonstrate the capabilities of the new dDAC setups at fast compression rates as it adopts a number of complex high pressure polymorphs at relatively low pressures, undergoing three 1st order phase transitions below 10 GPa.<sup>35</sup> Crucially, as it is a high-Z material, it is a strong x-ray scattering cross section and the LAMBDA detectors can be operated at the maximum collection rate, offering the best possible time resolution. Bi has been extensively studied using both static and dynamic compression techniques and has been shown to deviate from the equilibrium phase diagram under dynamic compression. In particular, a strain-rate dependent shift of the Bi-I/Bi-II phase boundary has been observed under dynamic loading with strain rates on the order of  $10^6$  s<sup>-1</sup> and metastable phases have been observed under shock compression.<sup>36,37</sup>

An example of a full compression-decompression cycle of Bi is shown in Fig. 7. In this experiment, Au was also loaded in the sample chamber as a pressure marker and the pressure was determined from the Au(111) diffraction peak using the EOS of Au from Ref. 38. Figure 7(a) shows a contour plot of the integrated diffraction patterns as a function of  $2\theta$  angle. The pressure ramp was designed



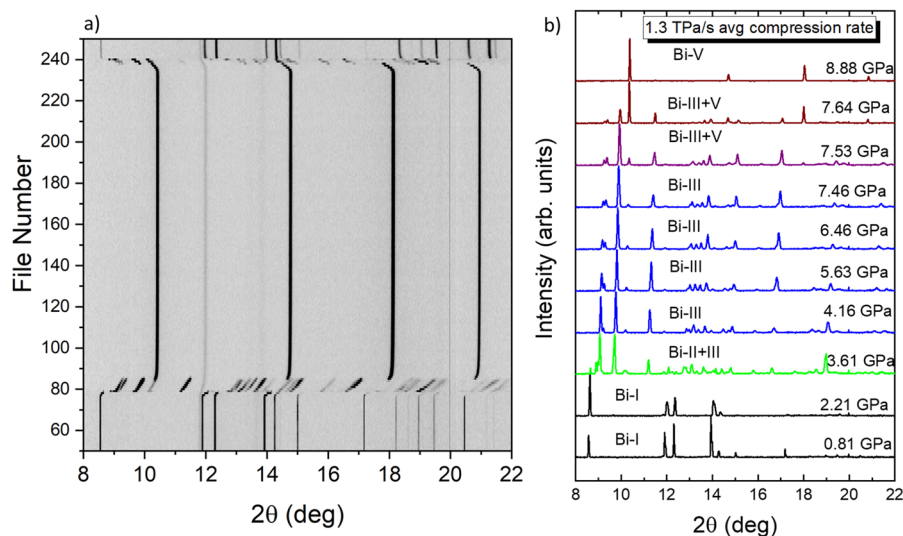


**FIG. 7.** (a) Integrated diffraction patterns of Bi and Au compressed from near ambient pressure to  $\sim 10$  GPa in 5 ms, and then released. (b) Stack of integrated diffraction patterns of consecutive exposures during compression, starting from 0.81 GPa in the stability field of Bi-I, and continuing through the phase transition sequence I-II-III-V. The pressure was determined based on the cell parameters and unit cell volume derived from the  $\text{Au}_{(111)}$  diffraction line using the EOS of Au.<sup>38</sup>

to be completed in 5 ms, during which time the sample pressure increased from 0.81 GPa to 8.88 GPa. The average compression rate for this ramp was determined to be 1.34 TPa/s. Figure 7(b) shows the integrated diffraction patterns collected during the ramp. Due to its narrow stability field, no single-phase diffraction patterns of monoclinic Bi-II were observed. Instead, traces of phase II were observed in the 3.16 GPa diffraction pattern alongside peaks from incommensurate Bi-III. Above this pressure, one observes single phase Bi-III patterns. At 7.53 GPa, weak peaks from the high symmetry bcc Bi-V are observed, and the transition from Bi-III to Bi-V is complete at 8.88 GPa.

Experiments at faster compression rates were performed using the LLNL 1-piezo-dDAC. In this case, Bi samples were loaded with Au into an  $\sim 15$   $\mu\text{m}$  thick stainless steel gasket on a 60  $\mu\text{m}$  culet beveled anvil and precompressed to an initial pressure of 3 GPa before compression. The voltage of the piezoactuator was increased from 0 to 1000 V in 2.5 ms, which resulted in an increase of the sample pressure to 152 GPa. This corresponds to an average compression rate of 59.6 TPa/s, with a maximum compression rate of 121.6 TPa/s. A plot of the pressure and compression rate vs time for the experiment is shown in Fig. 8. At these high compression rates, a large pressure increase occurs within a single exposure (500  $\mu\text{s}$ ) at the sampling rate of 2 kHz, and so structural changes which occur over narrow pressure regions cannot be resolved. In order to estimate the pressure increase during a single exposure at 100 TPa/s, the  $\text{Au}_{(111)}$  peak was fit using multiple Gaussian peaks with the full width at half maximum (FWHM) fixed to the FWHM at static pressure at the top of the ramp. The lowest-pressure peak position corresponds to a pressure of 10 GPa and the highest corresponds to 64 GPa, implying that more than 50 GPa was covered within a single diffraction pattern. The pressure plotted in Fig. 8 corresponds to that calculated from the centroid of the peak. This illustrates that in order to follow the crystal structure evolution at such high compression rates, one needs a higher brilliance x-ray beam and much faster detectors such as the AGIPD, both of which will soon be available at the High Energy Density Instrument at the European XFEL.

### C. Fast compression of low-Z compounds: $\text{H}_2\text{O}$

One may further utilize the capabilities of our dynamic compression setup for compressing low-Z compounds such as  $\text{H}_2\text{O}$ , which allows us to explore the stability and phase transition kinetics of the high-pressure polymorphs ice VI and VII. In these experiments, milli-Q  $\text{H}_2\text{O}$  was compressed from 0.5 to 20 GPa using the long 90 mm piezoactuator in the ECB dDAC, where the DAC was equipped with 0.3 mm culet diamond anvils.  $\text{H}_2\text{O}$  was contained in a stainless steel gasket indented to 0.025 mm and drilled with a 0.15 mm gasket hole. Properties of the incident x-ray beam and position of the LAMBDA detectors was identical to those described

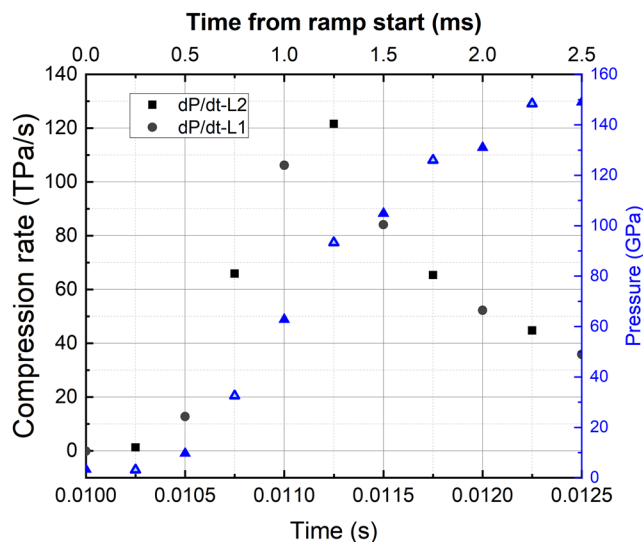


**FIG. 8.** Compression rate (black symbols) and pressure in the sample chamber (blue symbols) as a function of time for the compression of Bi in 60  $\mu\text{m}$  beveled diamonds. The pressure was determined based on the cell parameters and unit cell volume derived from the  $\text{Au}_{(111)}$  diffraction line using the EOS of Au.<sup>38</sup>

for the fast compression of gold, i.e., an  $8(\text{h}) \times 2(\text{v}) \mu\text{m}^2$  x-ray beam tuned to  $\sim 25.6$  keV. Diffraction images were collected on one LAMBDA detector with an exposure time of 200 ms and integrated in DIOPTAS as described above. Data were then processed using the customized beamline evaluation software “P02 Processing Tool.” In the experiment, Au powder (Sigma Aldrich, 326 585) was used as a pressure marker and the EoS of Anderson *et al.* was used to estimate the pressure using the Au(200) diffraction line.

A contour plot showing the time evolution of the integrated diffraction patterns during the compression experiment is shown in Fig. 9. The transition from ice VI to VII is clearly visible at  $\sim 2$  GPa. The average compression rate for the experiment in Fig. 9 was estimated to be 0.01 GPa/s. It is interesting to note that the pressure remained constant during the ice VI-VII transition, and that the compression rate increased slightly from 0.05 GPa/s in ice VI to 0.19 GPa/s in ice VII. The latter may be attributed to the slight change in bulk modulus when going from ice VI to ice VII.<sup>39</sup>

The integrated intensities of the strongest diffraction peak of ice VI(211) and ice VII(110) can be used to estimate the volume fraction of ice VI/ice VII as a function of time (Fig. 9). By fitting such a plot to an error function for a range of different compression rates, it is possible to estimate the activation volume of the ice VI to ice VII transition, thus allowing us to ascertain if nucleation is homogeneous or spontaneous when the sample is dynamically compressed in a DAC (Ref. 15). However, although these initial results are very promising, there are many experimental challenges that need to be addressed in future work. For example, the transition from ice VI to ice VII is characterized by the transformation of several crystallites as indicated by a very spotty diffraction pattern. This inherently means that the change of diffraction intensity of a given reflection during the compression may be influenced by rotation of the crystallites, changing the diffraction condition and consequently also the intensity of diffraction peak. Future experiments need to be designed in such a way that at least the ice VI diffraction images have a homogeneous intensity distribution across the Debye-Scherrer rings that is not biased by a change of crystallite rotations.

Another feature of the new dDAC diffraction setup is the improved diffraction resolution that originates from the small pixel

size of the LAMBDA detector and the consequent improved instrumental resolution. In the stability field of ice VII, high pressures have been shown to lead to a tetragonal distortion of the cubic crystal structure,<sup>40,41</sup> which is evident from the splitting of the ice VII(110) diffraction peak at 14 GPa. In our preliminary studies, ice VII was compressed up to a maximum pressure of 110 GPa with a compression rate of 0.8 GPa/s using the short 60 mm piezoactuator in the ECB dDAC. The splitting of the ice VII(110) diffraction peak has been seen on the GaAs LAMBDA detectors with a resolution that has not been reported before (Fig. 10) indicating that distortions in ice VII might occur at much lower pressure than previously observed.<sup>40</sup> Future work will have to confirm the validity of these initial observations as well as the role of varying compression rate on the formation of the distortions.

#### D. Pressure oscillation experiments

Another promising application of the dDAC is to subject samples to sinusoidal pressure oscillations at a wide range of frequencies (Fig. 11). With the high frame rates available using the LAMBDA detectors, x-ray diffraction patterns can be recorded at sufficiently high frequencies to resolve the mechanical response of the sample, e.g., the change in unit cell volume of the sample in an oscillating stress field. This approach offers a range of applications, including the potential to measure the elastic response of a sample under dynamic loading. Recently, the potential of this new approach was demonstrated by mapping out the spin transition-induced softening of the bulk modulus for ferropicicase ( $\text{Mg}_{0.8}\text{Fe}_{0.2}\text{O}$ ) (an iron content typical for the Earth's mantle) at 1 Hz seismic frequencies.<sup>42</sup> These results are highly relevant to the interpretation of seismic data of the lower mantle and will help to constrain its chemistry and thermal state.<sup>43</sup>

In the recent experiment, powder of ( $\text{Mg}_{0.8}\text{Fe}_{0.2}\text{O}$ ) ferropicicase was loaded along with platinum powder into symmetric piston cylinder type DAC, with 0.2 mm culets filled in the 0.1 mm wide and 0.03 mm thick gasket hole. The small ECB dDAC setup was used to compress the sample along a predefined path consisting of small increases of pressure followed by sinusoidal cycles around a constant pressure at 1 Hz frequencies (Fig. 11).

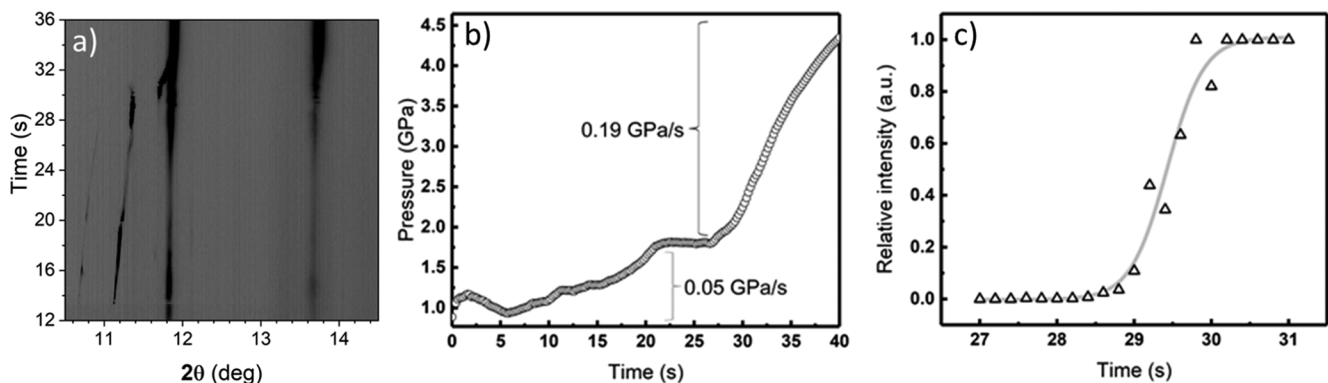


**FIG. 9.** Fast compression of  $\text{H}_2\text{O}$  depicting the transition from ice VI to ice VII. (a) Contour plot constructed from the integrated diffraction patterns collected on one of the LAMBDA detectors. (b) Plot of the pressure as a function of time for the compression experiment, where the pressure was determined from the Au(200) reflection based on the calibration by Anderson *et al.*<sup>30</sup> (c) Relative volume fraction going from ice VI to ice VII as a function of time.

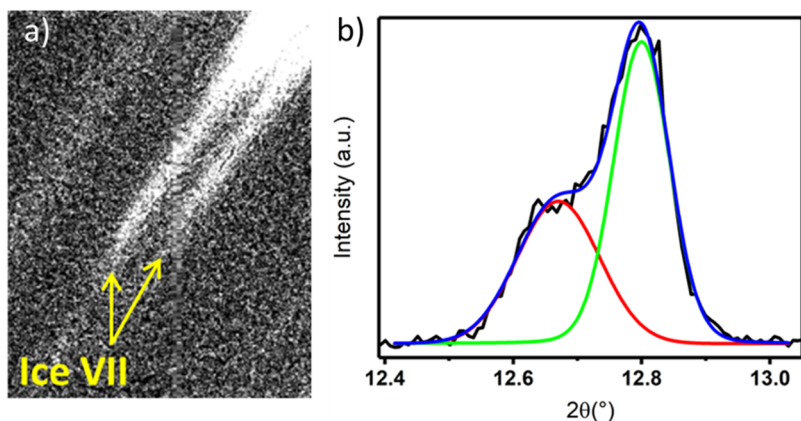


**FIG. 10.** Splitting of the ice VII(110) Bragg peak at 14 GPa. (a) Diffraction image collected on the 2M LAMBDA detectors showing the clear splitting of the ice VII(110) reflection. (b) Integrated diffraction profile showing the ice VII(110) peak, which has been fit as the sum of two Voigt functions to illustrate the splitting due to distortion of the cubic crystal structure.

Images were continuously recorded with a single image collection time of 5–50 ms, i.e., 20–200 images were collected within one oscillation at 1 Hz frequency. Data were automatically processed using the customized beamline evaluation software P02 Processing Tool. The resulting 2D diffraction patterns were used to estimate the bulk modulus of ferropericlyase, defined as  $K = -VdP/dV$ , which was derived for several pressures before, within, and after the spin transition region. Based on these experiments, it can be shown that the bulk modulus of ferropericlyase substantially softens across the spin transition, confirming previous measurements performed on single-crystals at very high frequencies.<sup>44</sup> Future work will exploit the capabilities of the dDAC cycling to derive the bulk modulus of a variety of crystalline substances of interest to earth science, materials science, and physics in a wide range of pressures.

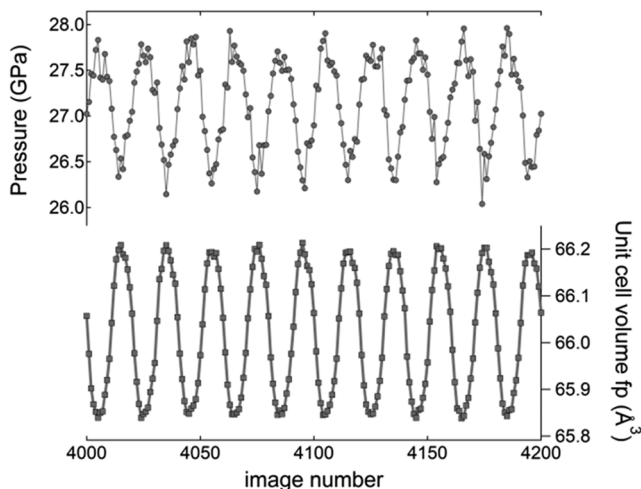


**FIG. 11.** Example of a pressure oscillation experiment carried out using the dDAC in combination with the LAMBDA detectors. Top panel: Pressure as determined from the Pt(111) line; bottom panel: Unit cell volume of ferropericlyase as derived from the  $F_{p200}$  line. The collection time for a single diffraction image was 50 ms. Oscillations were conducted at 1 Hz frequency. The material's bulk modulus can be directly derived from the data using its thermodynamic definition ( $K = -VdP/dV$ ); see also Refs. 37 and 42.

As part of our ongoing effort in dDAC development, both ECB and LLNL are currently developing a resistively-heated dDAC setup that is operated within a vacuum chamber, which will allow fast compression experiments at temperatures of up to 1500 K. This new setup will extend the oscillatory compression experiments to high temperatures and will thereby constitute the basis for future work on other materials that show anomalies in compressibility, e.g., when undergoing phase transitions.

## V. OUTLOOK

The examples above illustrate that fast compression in conjunction with x-ray diffraction of high-Z materials such as gold or bismuth at 100s of TPa/s, which is reaching the limit of what is technically possible in terms of dDAC technology, detector technology, and high energy brilliance provided by 3rd generation light sources. In the near future, it will be possible to further improve the detector technology by reducing the dynamic range of the GaAs 2.3 MP LAMBDA detector from 12 to 6 bit (or even lower) so that one can collect x-ray diffraction images at 4 kHz on each detector. However, it is already clear that the brilliance from the existing 3rd generation sources is insufficient to collect diffraction images of sufficient quality in many cases. One might look toward the new 4th generation storage rings such as the ESRF-BES, APS-U, or PETRA IV for an improvement in the brilliance of a factor of 10–100, but this is not sufficient to help with fast diffraction of low Z compounds. Ultimately, these experiments will have to be performed at 4th generation light sources such as the European XFEL that offer a better time resolution with pulses of 10–100 fs in length, pulse trains with repetition rates of 4.5 MHz, and brilliance at high x-ray energies of a factor of  $10^5$  better than any 3rd generation light source. For this reason, there is a concerted effort to further improve dDAC technology to reach compression rates beyond 100s of TPa/s and to develop dDAC setup for XFELs such as the High-Energy-Density (HED) Instrument of the European XFEL.

## VI. CONCLUSIONS

The development of a x-ray diffraction setup at the Extreme Conditions beamline (ECB, P02.2) for fast compression of samples

using different types of piezoactuator-driven dDACs has enabled a variety of new experimental capabilities that will influence the direction of research in the field of dynamic compression up to strain rates of  $10^2/s$  for years to come. In particular, the use of the new GaAs LAMBDA detectors enables the collection of x-ray diffraction images using the 25.6 keV incident x-ray beam at a repetition rate of up to 2 kHz using one detector and an effective rate of 4 kHz using two detectors.

**ACKNOWLEDGMENTS**

Portions (Zs.J., E.F.O., and W.E.) of this work were performed under the auspices of the US Department of Energy by the Lawrence Livermore National Laboratory under Contract No. DE-AC52-07NA27344. We acknowledge DESY (Hamburg, Germany), a member of the Helmholtz Association HGF, for the provision of experimental facilities. Parts of this research were carried out at PETRA III. Portions of this research were supported through the German Science Foundation DFG Research Unit FOR 2440 (Grant No. MA4534/5-1). Financial support by the BMBF (Grant No. 05K13RF1) and the DFG (Grant No. WI 1232) is gratefully acknowledged.

**APPENDIX: PRESSURE AS A FUNCTION OF APPLIED VOLTAGE IN THE DDAC WITH WATER TEST SAMPLE**

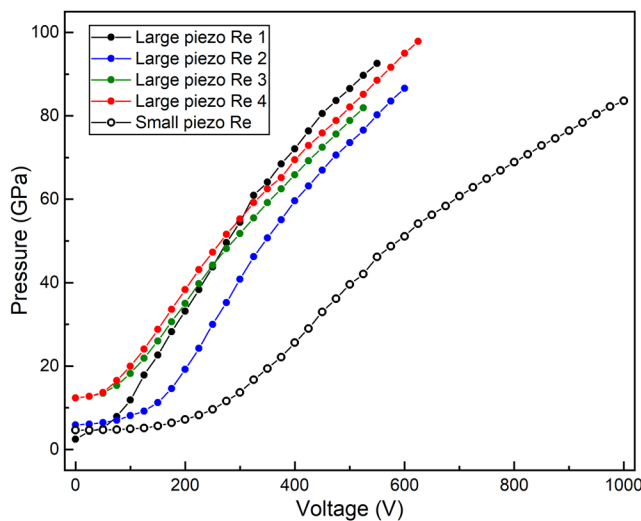


**FIG. 13.** Plot of pressure vs applied voltage for  $H_2O$  samples compressed in the ECB dDACs equipped with diamonds with  $200 \mu m$  culets and Re gaskets, illustrating the reproducibility of the dDAC. For the experiment performed using the small piezoactuator and experiment 1 with the large piezo, the pressure was determined using the ruby fluorescence method employing the calibration by Dewaele *et al.*<sup>24</sup> For compression performed using the large piezo (2–4), the pressure was determined from the Raman shift of the diamond phonons using the calibration by Akahama and Kawamura.<sup>25</sup>

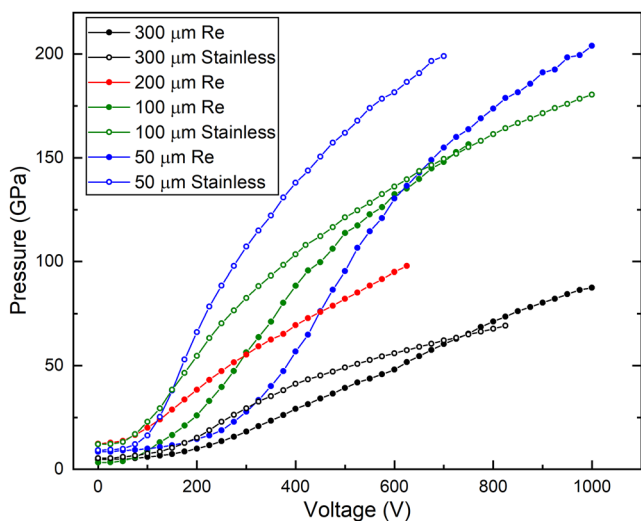


**FIG. 12.** Plot of pressure vs applied voltage for a  $H_2O$  sample compressed using ECB dDAC equipped with the large 90 mm piezoactuator (64-107), comparing the compression curves of samples compressed in Re and stainless steel gaskets for diamond anvils with different culet sizes. In most cases, the pressure was determined using the ruby fluorescence method employing the calibration by Dewaele *et al.*<sup>24</sup> For the  $50 \mu m$  culet diamonds and the  $100 \mu m$  culet diamonds with the stainless steel gasket, the pressure was determined from the Raman shift of the diamond phonon using the calibration by Akahama and Kawamura.<sup>25</sup> In some cases, the sample was not compressed up to maximum voltage due to diamond failure or loss of the ruby signal.

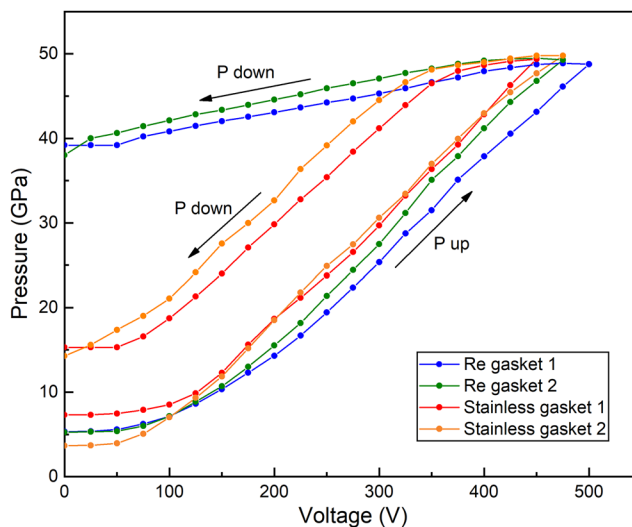


**FIG. 14.** Plot of pressure vs applied voltage for water samples compressed in the ECB dDAC with the large piezoactuator and diamonds with  $300 \mu m$  culets, illustrating the reproducibility of the dDAC for Re and stainless steel gaskets. For the experiment performed using the small piezo, the pressure was determined using the ruby fluorescence method employing the calibration by Dewaele *et al.*<sup>24</sup> For compression performed using the large piezo, the pressure was determined from the Raman shift of the diamond phonons using the calibration by Akahama and Kawamura.<sup>25</sup>



## REFERENCES

- <sup>1</sup>H.-K. Mao, X.-J. Chen, Y. Ding, B. Li, and L. Wang, *Rev. Mod. Phys.* **90**(1), 015007 (2018).
- <sup>2</sup>R. J. Angel, M. Bujak, J. Zhao, G. D. Gatta, and S. D. Jacobsen, *J. Appl. Crystallogr.* **40**, 26–32 (2007).
- <sup>3</sup>S. Klotz, J.-C. Chervin, P. Munsch, and G. Le Marchand, *J. Phys. D: Appl. Phys.* **42**, 075413 (2009).
- <sup>4</sup>N. Sata, G. Y. Shen, M. L. Rivers, and S. R. Sutton, *Phys. Rev. B* **65**(10), 104114 (2002).
- <sup>5</sup>W. J. Evans, C. S. Yoo, G. W. Lee, H. Cynn, M. J. Lipp, and K. Visbeck, *Rev. Sci. Instrum.* **78**(7), 073904 (2007).
- <sup>6</sup>G. W. Lee, W. J. Evans, and C.-S. Yoo, *Proc. Natl. Acad. Sci. U. S. A.* **104**(22), 9178–9181 (2007).
- <sup>7</sup>J.-Y. Chen and C.-S. Yoo, *Proc. Natl. Acad. Sci. U. S. A.* **108**(19), 7685–7688 (2011).
- <sup>8</sup>E.-R. Carl, U. Mansfeld, H.-P. Liermann, A. Danilewsky, F. Langenhorst, L. Ehm, G. Trullenque, and T. Kenkmann, *Meteorit. Planet. Sci.* **52**(7), 1465–1474 (2017).
- <sup>9</sup>E.-R. Carl, H.-P. Liermann, L. Ehm, A. Danilewsky, and T. Kenkmann, *Meteorit. Planet. Sci.* **53**(8), 1687–1695 (2018).
- <sup>10</sup>A. Cernok, K. Marquardt, R. Caracas, E. Bykova, G. Habler, H.-P. Liermann, M. Hanfland, M. Mezouar, E. Bobocioiu, and L. Dubrovinsky, *Nat. Commun.* **8**, 15647 (2017).
- <sup>11</sup>M. Sims, S. J. Jaret, E. R. Carl, B. Rhymer, N. Schrodt, V. Mohrholz, J. Smith, Z. Konopkova, H. P. Liermann, T. D. Glotch, and L. Ehm, *Earth Planet. Sci. Lett.* **507**, 166–174 (2019).
- <sup>12</sup>J. Y. Chen, C. S. Yoo, W. J. Evans, H. P. Liermann, H. Cynn, M. Kim, and Z. Jenei, *Phys. Rev. B* **90**(14), 144104 (2014).
- <sup>13</sup>J.-Y. Chen, M. Kim, C.-S. Yoo, H.-P. Liermann, and W. J. Evans, paper presented at the 18th Joint International Conference of the APS Topical Group on Shock Compression of Condensed Matter/24th International Conference of the International Association for the Advancement of High Pressure Science and Technology, Seattle, WA, 2013.
- <sup>14</sup>Z. Konopkova, A. Rothkirch, A. K. Singh, S. Speziale, and H.-P. Liermann, *Phys. Rev. B* **91**(14), 144101 (2015).
- <sup>15</sup>C. Lin, J. S. Smith, S. V. Sinogeikin, C. Park, Y. Kono, C. Kenney-Benson, E. Rod, and G. Shen, *J. Appl. Phys.* **119**(4), 045902 (2016).
- <sup>16</sup>S. V. Sinogeikin, J. S. Smith, E. Rod, C. Lin, C. Kenney-Benson, and G. Shen, *Rev. Sci. Instrum.* **86**(7), 072209 (2015).
- <sup>17</sup>J. S. Smith, S. V. Sinogeikin, C. Lin, E. Rod, L. Bai, and G. Shen, *Rev. Sci. Instrum.* **86**(7), 072208 (2015).
- <sup>18</sup>J.-Y. Chen and C.-S. Yoo, *J. Chem. Phys.* **136**(11), 114513 (2012).
- <sup>19</sup>D. Tomasino and C.-S. Yoo, *Appl. Phys. Lett.* **103**(6), 061905 (2013).
- <sup>20</sup>D. Pennicard, S. Smoljanin, F. Pithan, M. Sarajlic, A. Rothkirch, Y. Yu, H. P. Liermann, W. Morgenroth, B. Winkler, Z. Jenei, H. Stawitz, J. Becker, and H. Graafsma, *J. Instrum.* **13**, C01026 (2018).
- <sup>21</sup>Z. Jenei, H. Cynn, K. Visbeck, and W. J. Evans, *Rev. Sci. Instrum.* **84**(9), 095114–095116 (2013).
- <sup>22</sup>E. F. O'Bannon III, Z. Jenei, H. Cynn, M. J. Lipp, and J. R. Jeffries, *Rev. Sci. Instrum.* **89**(11), 111501 (2018).
- <sup>23</sup>E. Wittich, Bachelors Thesis, Hamburg University of Applied Sciences, 2013.
- <sup>24</sup>A. Dewaele, P. Loubeyre, and M. Mezouar, *Phys. Rev. B* **70**(9), 094112 (2004).
- <sup>25</sup>Y. Akahama and H. Kawamura, *J. Appl. Phys.* **100**(4), 043516 (2006).
- <sup>26</sup>R. Ballabriga, J. Alozy, G. Blaj, M. Campbell, M. Fiederle, E. Frojdh, E. H. M. Heijne, X. Llopart, M. Pichotka, S. Procz, L. Tlustos, and W. Wong, *J. Instrum.* **8**, C02016 (2013).
- <sup>27</sup>E. Hamann, T. Koenig, M. Zuber, A. Cecilia, A. Tyazhev, O. Tolbanov, S. Procz, A. Fauler, T. Baumbach, and M. Fiederle, *IEEE Trans. Med. Imaging* **34**(3), 707–715 (2015).
- <sup>28</sup>C. Prescher and V. B. Prakapenka, *High Pressure Res.* **35**(3), 223–230 (2015).
- <sup>29</sup>H. P. Liermann, Z. Konopkova, W. Morgenroth, K. Glazyrin, J. Bednarcik, E. E. McBride, S. Petitgirard, J. T. Delitz, M. Wendt, Y. Bican, A. Ehn, I. Schwark, A. Rothkirch, M. Tischer, J. Heuer, H. Schulte-Schrepping, T. Kracht, and H. Franz, *J. Synchrotron Radiat.* **22**, 908–924 (2015).
- <sup>30</sup>O. L. Anderson, D. G. Isaak, and S. Yamamoto, *J. Appl. Phys.* **65**(4), 1534–1543 (1989).
- <sup>31</sup>A. K. Singh, H. P. Liermann, and S. K. Saxena, *Solid State Commun.* **132**(11), 795–798 (2004).
- <sup>32</sup>H. P. Liermann, A. K. Singh, B. Manoun, S. K. Saxena, and C. S. Zha, *Int. J. Refract. Met. Hard Mater.* **23**(2), 109–114 (2005).
- <sup>33</sup>C. G. Schroer, I. Agapov, W. Brefeld, R. Brinkmann, Y.-C. Chae, H.-C. Chao, M. Eriksson, J. Keil, X. N. Gavalda, R. Roehlsberger, O. H. Seeck, M. Sprung, M. Tischer, R. Wanzenberg, and E. Weckert, *J. Synchrotron Radiat.* **25**, 1277–1290 (2018).
- <sup>34</sup>T. S. Duffy and R. F. Smith, *Front. Earth Sci.* **7**, 23 (2019).
- <sup>35</sup>O. Degtyareva, M. I. McMahan, and R. J. Nelmes, *High Pressure Res.* **24**(3), 319–356 (2004).
- <sup>36</sup>R. F. Smith, J. H. Eggert, M. D. Saculla, A. F. Jankowski, M. Bastea, D. G. Hicks, and G. W. Collins, *Phys. Rev. Lett.* **101**(6), 065701 (2008).
- <sup>37</sup>M. G. Gorman, A. L. Coleman, R. Briggs, R. S. McWilliams, D. McGonegle, C. A. Bolme, A. E. Gleason, E. Galtier, H. J. Lee, E. Granados, M. Sliwa, C. Sanloup, S. Rothman, D. E. Fratanduono, R. F. Smith, G. W. Collins, J. H. Eggert, J. S. Wark, and M. I. McMahan, *Sci. Rep.* **8**, 16927 (2018).
- <sup>38</sup>Y. Fei, A. Ricolleau, M. Frank, K. Mibe, G. Shen, and V. Prakapenka, *Proc. Natl. Acad. Sci. U. S. A.* **104**(22), 9182–9186 (2007).
- <sup>39</sup>A. D. Fortes, I. G. Wood, M. G. Tucker, and W. G. Marshall, *J. Appl. Crystallogr.* **45**, 523–534 (2012).
- <sup>40</sup>M. Somayazulu, J. F. Shu, C. S. Zha, A. F. Goncharov, O. Tschauer, H. K. Mao, and R. J. Hemley, *J. Chem. Phys.* **128**(6), 064510 (2008).
- <sup>41</sup>H. Hirai, H. Kadobayashi, T. Matsuoka, Y. Ohishi, and Y. Yamamoto, *High Pressure Res.* **34**(3), 289–296 (2014).
- <sup>42</sup>H. Marquardt, J. Buchen, A. S. J. Mendez, A. Kurnosov, M. Wendt, A. Rothkirch, D. Pennicard, and H.-P. Liermann, *Geophys. Res. Lett.* **45**(14), 6862–6868, <https://doi.org/10.1029/2018gl077982> (2018).
- <sup>43</sup>J.-F. Lin, S. Speziale, Z. Mao, and H. Marquardt, *Rev. Geophys.* **51**(2), 244–275, <https://doi.org/10.1002/rog.20010> (2013).
- <sup>44</sup>J. C. Crowhurst, J. M. Brown, A. F. Goncharov, and S. D. Jacobsen, “Elasticity of (Mg, Fe) O through the spin transition of iron in the lower mantle,” *Science* **319**(5862), 451–453 (2008).